

## Generalized functional model of maximum and minimum detectable deformation gradient for PALSAR interferometry

Qi-jie WANG<sup>1</sup>, Zhi-wei LI<sup>1</sup>, Ya-nan DU<sup>1</sup>, Rong-an XIE<sup>2</sup>, Xin-qing ZHANG<sup>2</sup>, Mi JIANG<sup>1</sup>, Jian-jun ZHU<sup>1</sup>

1. School of Geoscience and Info-Physics Engineering, Central South University, Changsha 410083, China;

2. Geology Surveying and Mapping Institute of Guangdong Province, Guangzhou 510800, China

Received 17 September 2013; accepted 23 December 2013

**Abstract:** Empirical functional models for the maximum and minimum detectable deformation gradient of PALSAR interferometry were established based on coherence and discrete look numbers. Then, a least square regression method was used to fit the model coefficients and thus obtain the generalized functional models for both coherence and look numbers. The experimental results with ALOS PALSAR data of Wenchuan earthquake of China show that the new model works well for judging whether the deformation gradient can be detected by the D-InSAR technology or not. The results can help researchers to choose PALSAR data and to configure processing parameters, and also benefit the interpretation of the measured surface deformation.

**Key words:** PALSAR; D-InSAR; deformation gradient; coherence; multilook number; functional model

### 1 Introduction

Phased array type L-band synthetic aperture radar (PALSAR) is an L-band SAR imaging sensor, which can overcome the decorrelation better than the C-band one, and thus has been widely used for ground deformation monitoring [1–3]. However, not all the deformations can be detected by D-InSAR technology, due to the limitation of the hardware and the interferometric noise caused by temporal and geometrical decorrelation and atmospheric delay, etc [4–6]. Excessive ground deformations cannot be detected because of the interferometric decorrelation or the phase aliasing [7], while the very small deformations can be screened by atmospheric noise or orbital residual phase [8]. Modeling the minimum and maximum detectable deformation gradient (DDG) of D-InSAR is important, as it can be used to judge whether the surface deformation can be detected or not in advance. It has a great significance on the accurate selection of monitoring objects, radar data and the reasonable configuration of interferometric parameters.

MASSONNET and FEIGL [8] first investigated the maximum DDG model, and implied that the maximum

DDG (either moving towards or away from the satellite) was one fringe per pixel, as defined by

$$D = \frac{\lambda}{2\mu} \quad (1)$$

where  $\lambda$  is the radar wavelength;  $\mu$  is the pixel size.  $D$  is dimensionless in the definition. However, the maximum detectable deformation is usually below this value due to the effects of interferometric noise, which are caused by temporal-spatial decorrelation and atmosphere delays.

To circumvent this, BARAN et al [9] analyzed the relationship between the detectable deformation gradient and the coherence through simulated experiments, and proposed a coherence-based empirical functional model of the maximum and minimum DDG for ASAR sensor

$$\begin{cases} D_{\max}(\gamma) = 0.0014 + 0.002(\gamma - 1) \\ D_{\min}(\gamma) = -0.00007(\gamma - 1) \end{cases} \quad (2)$$

where  $D_{\max}$  and  $D_{\min}$  are the maximum and minimum detectable deformation gradients, respectively. As the phase noise in an interferogram is a function of both the interferometric coherence and the look number used in multi-look operation [10], the BARAN model is not comprehensive because it considers only the interferometric coherence. JIANG and LI [11] extended

the empirical functional model to incorporate both factors, but they only established the models of look numbers  $L=1, 5$  and  $20$  for ASAR sensor,

$$\begin{cases} D_{\max}(\gamma, L=1) = 0.0114(\gamma-1) + 0.007 \\ D_{\min}(\gamma, L=1) = -0.0002(\gamma-1) + 1 \times 10^{-7} \\ D_{\max}(\gamma, L=5) = 0.002(\gamma-1) + 0.0014 \\ D_{\min}(\gamma, L=5) = -0.00008(\gamma-1) + 1 \times 10^{-7} \\ D_{\max}(\gamma, L=20) = 0.0009(\gamma-1) + 0.0007 \\ D_{\min}(\gamma, L=20) = -0.000034(\gamma-1) + 1 \times 10^{-7} \end{cases} \quad (3)$$

From the above analysis, we can see that the existing researches all focus on ASAR platform, and there are no researches on PALSAR sensor. On the other hand, the existing models are only applicable to some special look numbers and no generalized functional models exist currently. To solve these problems, this work will construct the generalized functional models of the maximum and minimum DDG for PALSAR sensor. Firstly, the empirical models of the minimum and maximum DDG are established for look numbers  $L=3, 12$  and  $24$ . Then, the empirical models are extended to general look numbers and the generalized functional models of the maximum and minimum DDG are built. Finally, the developed models are validated with real PALSAR data. The results can not only offer guidance for choosing appropriate monitoring objects and configuring interferometric parameters, but also benefit the interpretation of the surface deformation measured by PALSAR.

## 2 Construction of maximum and minimum DDG models for PALSAR

### 2.1 Research methods

The flowchart in Fig. 1 outlines the method applied in this study. First, representative surface deformations with varying spatial extents and magnitudes are simulated and converted into deformation phases.

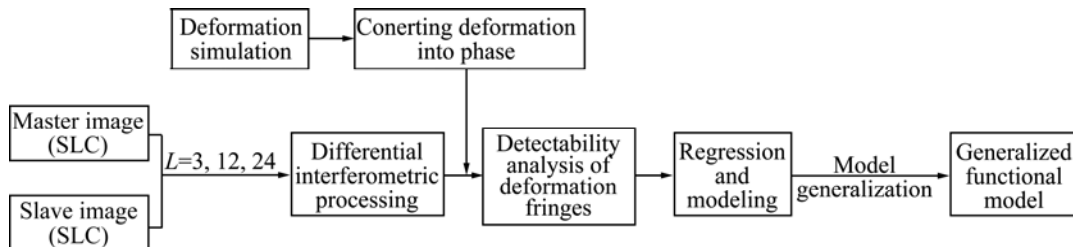


Fig. 1 Flowchart of research method

Second, a pair of PALSAR images that contain different levels of phase noise are selected and processed to obtain differential interferogram, and then the simulated phases are added into the differential interferogram. Third, the empirical minimum and maximum DDG models are established for common look numbers  $L=3, 12$  and  $24$ , respectively. Finally, empirical models for other look numbers are established and then generalized to establish the uniform minimum and maximum DDG models.

### 2.2 PALSAR data and study area

PALSAR is carried on the Advanced Land Observing Satellite (ALOS) that was launched on January 24, 2006. PALSAR is a fully polarimetric instrument, which operates in L-band with 14 and 28 MHz bandwidths and 1270 MHz (23.6 cm) center frequency, and can be operated in five different observation modes: Fine Beam Dual (FBD) polarization, Fine Beam Single (FBS) polarization, Polarimetric (POL) mode, ScanSAR mode and Direct Transmission (DT) mode [12]. The data used in this work is a 1.0 level product in FBS mode, whose incident angle is  $38.7^\circ$ , swath width is 70 km and the range and azimuth resolutions are 4.684 m and 3.155 m, respectively.

In order to reduce the influence of surface deformation and topographic relief, SAR pair with small temporal and spatial baselines is preferred. In addition, the weather and vegetation coverage of the experimental area should be dry and subtle in order to reduce the influence of other factors. Jointly considering these factors, a pair of ascending PALSAR images covering Bam, Iran are chosen, with a 46 temporal baseline. Table 1 shows the detailed information of the SAR pair.

### 2.3 Deformation simulation

Ground subsidence in a local area often has a “bowl” shape [13–15] and two-dimension elliptical Gaussian function is generally used to model it,

Table 1 Parameters of selected SAR pair

Image	Date	Frame	Track	Central latitude and longitude	Spatial baseline/m	Temporal baseline/d	Incidence/(°)	Mode
Master	March 1, 2010	21847	560	29.215°N	125.03	46	38.7	FBS
Slave	April 16, 2010	22518	560	58.356°E				

$$f(x, y) = \frac{1}{2\pi\sigma_x\sigma_y} \exp\left\{-\frac{1}{2}\left[\frac{(x-\mu_x)^2}{\sigma_x^2} + \frac{(y-\mu_y)^2}{\sigma_y^2}\right]\right\} \quad (4)$$

where  $x$  and  $y$  represent the coordinates in the range and azimuth directions, respectively;  $\mu_x$  and  $\mu_y$  are the means;  $\sigma_x$  and  $\sigma_y$  are the standard deviations of the simulated deformation in the range and azimuth directions, respectively.  $f(x, y)$  is the simulated deformation along the radar LOS. Deformations with different spatial extents can be obtained by altering the values of  $\sigma_x$  and  $\sigma_y$ . By scaling  $f(x, y)$ , the final simulated deformations with different amplitudes can be obtained. For simplicity, it is assumed that the deformation in the vertical direction equals that in LOS direction. Table 2 shows two groups of the simulated deformations as denoted by group I and group II, respectively. Both groups have 9 ground subsidences with a spatial extent of 960 m×480 m and 600 m×360 m in the azimuth and range directions, respectively. Each simulated deformation represents a unique deformation gradient.

**Table 2** Models of simulated deformations

Group I	A1	B1	C1	D1	E1	F1	G1	H1	I1
Fringe	1/8	1/4	1/2	1	2	2.5	3	3.5	4
Deformation/cm	1.5	3	5.9	11.8	23.6	29.5	35.4	41.3	47.2
Deformation gradient/ $10^{-4}$	0.63	1.25	2.5	4.9	9.8	12.3	14.8	17.2	19.7
Azimuth×range/m	960×480								
Group II	A2	B2	C2	D2	E2	F2	G2	H2	I2
Fringe	1/8	1/4	1/2	1	2	2.5	3	3.5	4
Deformation/cm	1.5	3	5.9	11.8	23.6	29.5	35.4	41.3	47.2
Deformation gradient/ $10^{-4}$	0.8	1.7	3.3	6.5	13.1	16.4	19.7	22.9	26.2
Azimuth×range/m	600×360								

## 2.4 Interferometric processing

Conventional two-pass differential interferometry approach is used in this work. During the SAR data processing, the 90-m Shuttle Radar Topography Mission digital elevation model is used to remove the topographic phase. Firstly, 20 patches are chosen in the single-look differential interferogram. The selection of the patches should ensure that the mean coherences within them are approximately uniformly distributed, i.e., ranging from 0 to 1, so that the samples are comprehensive. Both groups in Table 2 include 9 surface deformations with different spatial extents, which thus represent 18 deformation gradients. For each deformation gradient, it is converted into deformation phase and it is added into the 20 selected interferogram patches with different look numbers. The detectability of the simulated deformation phases in each of the patches is then analyzed according to the method described in the next section. Finally, this

operation is repeated until all the 18 deformation gradients are gone through.

## 2.5 Detectability analysis

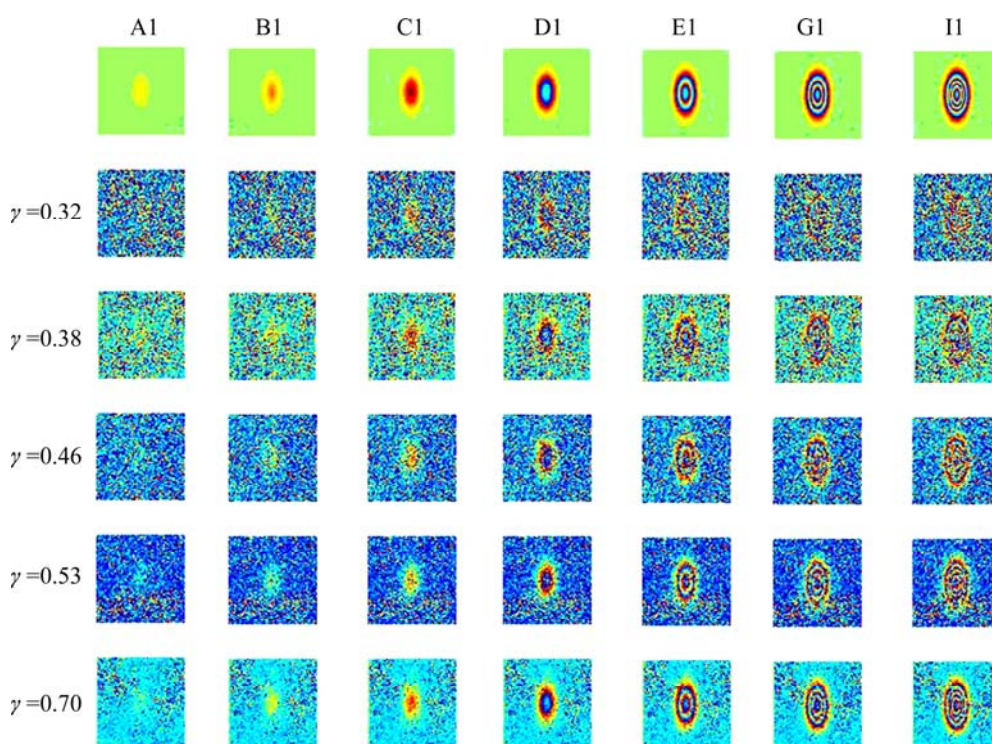
A visual inspection method is adopted in this work to determine whether the simulated deformations can be detected or not, due to the lack of well-developed numerical methods. Figure 2 shows the relationship between the coherence and the DDG when the look number  $L=3$ , in which the mean coherences range from 0.3 to 0.7. It can be seen from Fig. 2 that with the increase of the coherence, the detectability of the simulated deformations is enhanced (along column direction). For example, when  $\gamma=0.32$ , the outlines of model D1 (one fringe) are not clear in the differential interferogram. However, it becomes clearer and clearer with the increase of the coherence. In the row direction, the outlines of the fringes become clearer with the increase of the deformation gradients, although it may become more and more difficult to determine the number of the fringes. For example, when the mean coherence  $\gamma=0.46$ , the outlines of model D1 (one fringe) in the differential interferogram are clearer than those of model C1 (half fringe), and with the increase of the deformation gradient (model I1) the outlines become clearer but the fringe number is difficult to figure at the same time.

Figure 3 shows the relationship between look numbers and DDG in the same patch, where the mean coherence  $\gamma=0.42$ . The results in Fig. 3 indicate that for models with small deformation gradients and sparse fringes (e.g., B1, C1 and D1), the influence of interferometric noise becomes subtler with the increase of look number, and the outlines of the deformation become clearer. While for models with larger deformation gradients and denser fringes (e.g., G1 and H1), the deformation information can be destroyed due to the over-large look number ( $L=24$ ), where phase aliasing can be observed. However, appropriate multi-look operation ( $L=3$ ) can reduce the influence of noise and make the deformation detectable at the same time.

As noted earlier, DDG is a function of pixel size, and different pixel sizes in range and azimuth directions result in different DDG. The detectability in the two directions will be comprehensively considered and a reasonable judgment will be given based on the closure nature of the fringes.

## 2.6 Maximum and minimum DDG model for PALSAR

For look numbers  $L=3, 12$  and  $24$ , the detectability of the 18 deformation gradients is analyzed, and added into the 20 selected patches one by one. Linear regression analysis is used to fit the lower and upper



**Fig. 2** Differential interferogram patches of different coherences after adding deformation models of group I (The look number  $L=3$ . The pixel size is about  $9.465\text{ m}\times 7.9\text{ m}$ )

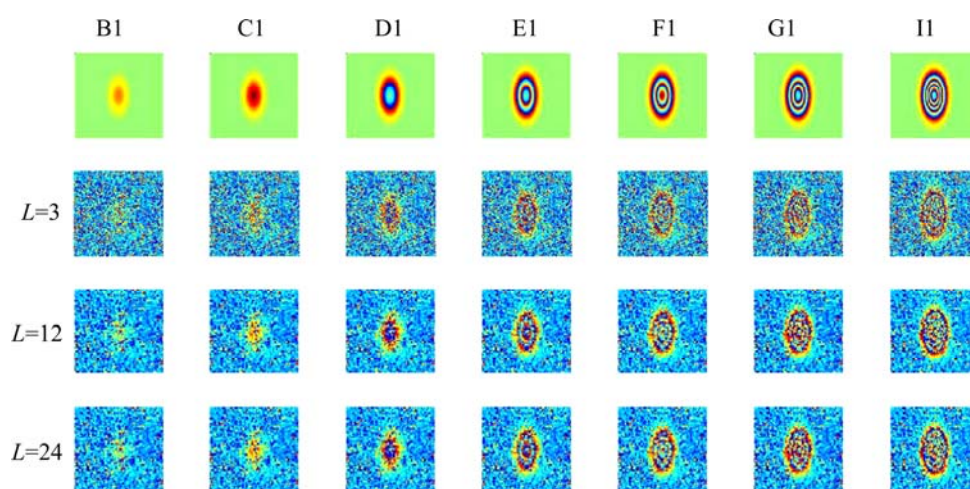


**Fig. 3** Differential interferogram patches of different look numbers after adding deformation models of group I (The mean coherence of these patches is 0.42, the look numbers are  $L=3, 12, 24$ , respectively, and their corresponding pixel sizes are  $7.9\text{ m}\times 9.465\text{ m}$ ,  $15.8\text{ m}\times 18.93\text{ m}$  and  $23.7\text{ m}\times 25.24\text{ m}$ , respectively)

bounds of the DDG for each look number. Figure 4 shows the scatter plots of the detectability except those whose detectabilities are difficult to decide based on visual analysis. Red asterisks and blue dots represent the detectable and undetectable deformation, respectively.

The results in Fig. 4 indicate that there are obvious differences in the detectabilities for different look numbers. The maximum DDG becomes smaller with the increase of look number. This is because large deformation gradient results in denser interferometric

fringe and tends to cause phase aliasing with over-large look number (Fig. 3). Conversely, the minimum DDG becomes larger with the increase of look number, because for small deformation gradient, more phase noises are removed with a large look number, while the phase aliasing doesn't happen.

It can be concluded that the relationship among coherence and upper and lower bounds of the DDG is approximately linear from Fig. 4. Moreover, the constraints of D-InSAR technology are taken into

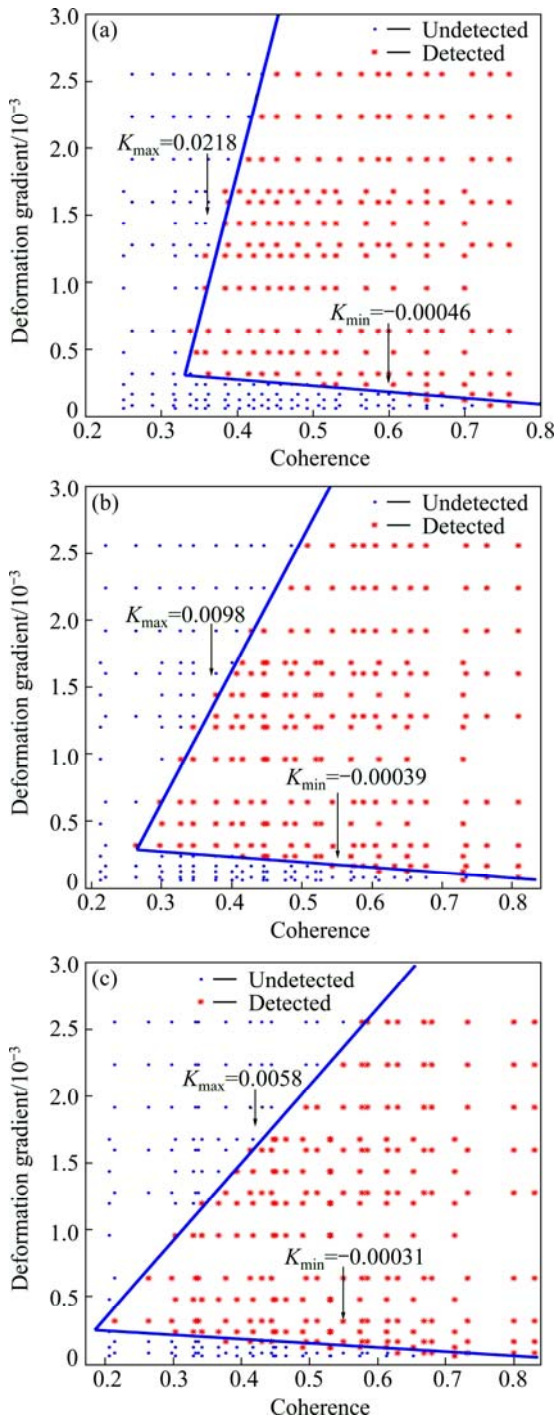


**Fig. 4** Statistical results of detectability for look numbers  $L=3$  (a), 12 (b) and 24 (c)

account, namely, the maximum DDG equals  $D_L$  and the minimum DDG equals  $10^{-7}$  when coherence  $\gamma=1$  [8]. Therefore, the following linear functions can be used to fit the maximum and minimum DDG models:

$$\begin{cases} D_{\max}(\gamma, L) = K_{\max, L} \times (\gamma - 1) + D_L \\ D_{\min}(\gamma, L) = K_{\min, L} \times (\gamma - 1) + 10^{-7} \end{cases} \quad (5)$$

where  $K_{\max, L}$  and  $K_{\min, L}$  represent the slope of the linear models.

$K_{\max, L}$  and  $K_{\min, L}$  are estimated using the observation samples in Fig. 4 and  $D_L$  is calculated through Eq. (1). The maximum and minimum DDG models thus established for PALSAR and look numbers  $L=3, 12$  and  $24$  are

$$\begin{cases} D_{\max}(\gamma, L=3) = 0.0212(\gamma - 1) + 0.0149 \\ D_{\min}(\gamma, L=3) = -0.000814(\gamma - 1) + 1 \times 10^{-7} \\ D_{\max}(\gamma, L=12) = 0.0093(\gamma - 1) + 0.00747 \\ D_{\min}(\gamma, L=12) = -0.00062(\gamma - 1) + 1 \times 10^{-7} \\ D_{\max}(\gamma, L=24) = 0.0057(\gamma - 1) + 0.005 \\ D_{\min}(\gamma, L=24) = -0.00051(\gamma - 1) + 1 \times 10^{-7} \end{cases} \quad (6)$$

### 3 Generalization of maximum and minimum DDG model for PALSAR

The models in Eq. (6) can only be applied to look numbers  $L=3, 12$  and  $24$ , and are generalized to incorporate more general look numbers in this section. For each look number, three model parameters are fitted,  $D_L, K_{\max, L}$  and  $K_{\min, L}$ , from the detectability observations in the 20 selected interferometric patches. To better describe their relationship with look number, they are modified to the format of  $D(L), K_{\max}(L)$  and  $K_{\min}(L)$ , respectively. Thus, the generalized model becomes

$$\begin{cases} D_{\max}(\gamma, L) = D(L) + (\gamma - 1) \times K_{\max}(L) \\ D_{\min}(\gamma, L) = 1 \times 10^{-7} + (\gamma - 1) \times K_{\min}(L) \end{cases} \quad (7)$$

In order to determine  $K_{\max}(L)$  and  $K_{\min}(L)$ ,  $(L, K_{\max}(L))$  and  $(L, K_{\min}(L))$  are plotted in a two-dimensional coordinate system, but the results show that the scatter plots cannot be represented with a simple curve. As noted earlier, the deformation gradient is a function of radar wavelength and pixel size, and the pixel size can be altered with different multi-look numbers. To avoid contradiction, the smaller pixel size ( $J$ ) is used to estimate the gradient as a convention when the azimuth and range size are different. At this stage, the relationship can be established among  $K_{\max}(L), K_{\min}(L)$  and look number  $L$ .

However, not all the look numbers can be realized in real interferometric processing, and it is common to select look numbers that tend to make the shape of a pixel close to a ‘square’. Therefore, the selection of look number  $L$  is of great importance. Three rules will be applied in this work for look number selection. First, those look numbers that cannot be decomposed are excluded, such as  $L=7, 11, 13, 17, 19$ . Second, in order to get an optimal relationship between the smaller pixel size and the look number, some look numbers are removed to ensure the pixel size monotone increasing with look number. For example, when look number  $L=10$  and  $12$ , the small pixel sizes are both  $J=15.8$ . Thus the look

number  $L=10$  is excluded because the shape of the final pixel is more close to a square when look number  $L=12$ . Third, the look number  $L=1$  is excluded, because of the incorrect co-registration between the interferogram and the simulated topographic phase from 90-m SRTM due to their big differences in resolutions. Eventually, 8 look numbers are obtained which will be used to derive the generalized model. Table 3 shows the smaller pixel size for each look number. An empirical relationship between  $J$  and  $L$  can be established.

$$J(L) = \begin{cases} 3.148L/\sqrt{L/3} & (L = 3, 12, 24) \\ 7.9\text{ceil}(\sqrt{L/3}) & (L = 2, 6, 8, 18, 21) \end{cases} \quad (8)$$

where  $\text{ceil}(x)$  gives an integer equal to or just greater than  $x$ .

**Table 3** Smaller pixel size for different look numbers

Look number	$L=2$	$L=3$	$L=6$	$L=8$	$L=12$	$L=18$	$L=21$	$L=24$
$J/m$	6.296	7.900	9.444	12.592	15.800	18.888	22.036	23.700

**3.1 Generalized model of maximum DDG for PALSAR**

$D(L)$  can be simply estimated based on Eq. (1) and  $J(L)$ ,

$$D(L) = \frac{\lambda}{2J(L)} \quad (9)$$

To investigate the functional relationship between  $J(L)$  and  $K_{\max}(L)$ , the scatter plots of  $J(L)$  versus  $K_{\max}(L)$  (see Table 4) are shown in Fig. 5.

**Table 4**  $K_{\max}$  and its estimated  $K_{\max\_es}$  for different look number

Look number	$L=2$	$L=3$	$L=6$	$L=8$	$L=12$	$L=18$	$L=21$	$L=24$
$K_{\max}/10^{-3}$	28.4	21.2	17.7	12.6	9.8	7.9	6.4	5.8
$K_{\max\_es}/10^{-3}$	27.9	21.8	17.8	12.8	9.8	7.8	6.3	5.7

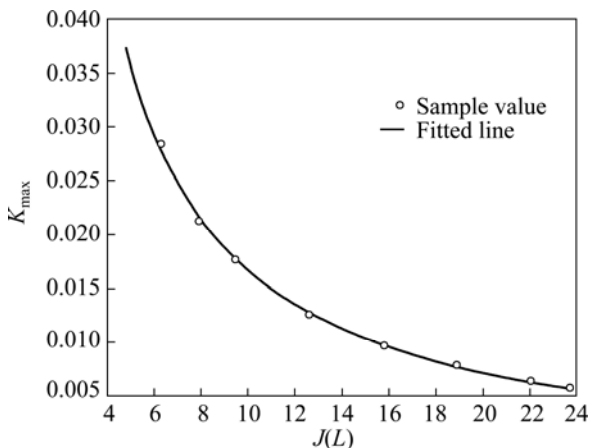


**Fig. 5** Least square fitting of  $K_{\max}$  with respect to  $J(L)$

From Fig. 5, it is clear that  $K_{\max}(L)$  decreases with  $J(L)$ , and its trend is close to the model  $y=a/x+b$ . The method of least square regression is applied to fitting the model. The fitted curve is also shown in Fig. 5 for comparison. It is clear that it matches the samples very well. The fitted slopes  $K_{\max\_es}$  are also listed in Table 4, which are very close to  $K_{\max}(L)$  too. Thus,  $K_{\max}(L)$  can be expressed as

$$K_{\max}(L) = 0.1903 \times \frac{1}{J(L)} - 2.286 \times 10^{-3} \quad (10)$$

Combining Eqs. (7) and (10), the generalized maximum DDG model for PALSAR can be obtained as

$$D_{\max}(\gamma, L) = \frac{\lambda}{2J(L)} + (0.1903 \times \frac{1}{J(L)} - 2.286 \times 10^{-3}) \times (\gamma - 1) \quad (11)$$

**3.2 Generalized model of minimum DDG for PALSAR**

The generalized model of the minimum DDG for PALSAR will be estimated using the same method described above. Figure 6 shows the scatter plots of  $J(L)$  versus  $K_{\min}(L)$ .

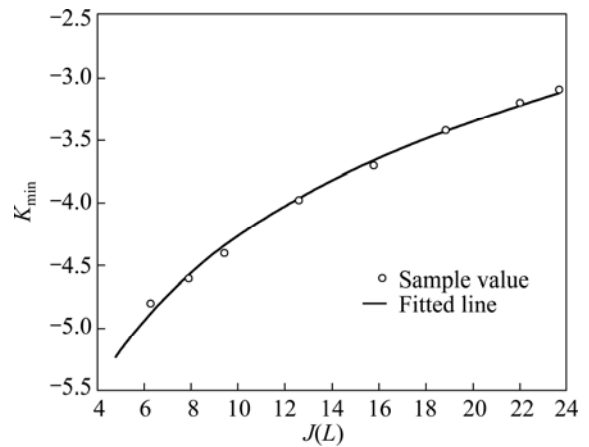


**Fig. 6** Least square fitting of  $K_{\min}$  with respect to  $J(L)$

Figure 6 shows that  $K_{\min}(L)$  increases with  $J(L)$ , and its trend is close to the logarithm function model  $y=a \ln x+b$ . The method of least squares regression is applied to fit the model. The fitted curve is also shown in Fig. 6, and Table 5 shows the fitted slopes  $K_{\min\_es}$ , both indicating a very well fitting conducted. Thus,  $K_{\min}(L)$  can be expressed as

$$K_{\min}(L) = 1.317 \times 10^{-4} \ln J(L) - 7.301 \times 10^{-4} \quad (12)$$

Combining Eqs. (7) and (12), the generalized model of the minimum DDG for PALSAR reads

$$D_{\min}(\gamma, L) = 1 \times 10^{-7} + [1.317 \times 10^{-4} \ln J(L) - 7.301 \times 10^{-4}] \times (\gamma - 1) \quad (13)$$

**Table 5**  $K_{\min}$  and its estimated  $K_{\min\_es}$  for different look numbers

Look number	$L=2$	$L=3$	$L=6$	$L=8$	$L=12$	$L=18$	$L=21$	$L=24$
$K_{\min}/10^{-4}$	4.8	4.6	4.4	3.98	3.7	3.42	3.2	3.1
$K_{\min\_es}/10^{-4}$	4.87	4.58	4.34	3.96	3.67	3.43	3.21	3.13

Finally, the generalized functional model of the maximum and minimum DDG for PALSAR based on coherence and look number can be summarized from Eqs. (8), (11) and (13):

$$\begin{cases} D_{\max}(\gamma, L) = \frac{\lambda}{2J(L)} + (0.1903 \times \frac{1}{J(L)} - 2.286 \times 10^{-3}) \times (\gamma - 1) \\ D_{\min}(\gamma, L) = 1 \times 10^{-7} + [1.317 \times 10^{-4} \ln J(L) - 7.301 \times 10^{-7}] \times (\gamma - 1) \end{cases} \quad (14)$$

The generalized functional model is more practical and accurate, and applicable in a wider range. It correctly reduces to Eq. (6) when the look numbers  $L=3, 12$  and  $24$ , and to the Massonnet’s model when the coherence value  $\gamma=1$ .

**4 Model validation**

An PALSAR pair (Track: 474) acquired on March 5 and June 5, 2008 covering Wenchuan, China, is used to validate the proposed model. The spatial and temporal baselines are 226 m and 46 d, respectively. The PALSAR pair is processed with the two-pass D-InSAR method, where the 90-m SRTM is used to remove the topographic phase. Three look numbers  $L=3, 12$  and  $24$  are adopted in the processing. Figure 7 shows the geocoded differential interferogram, in which a representative patch marked by a green square, is selected to examine whether the DDG models are able to detect the deformation gradients at given look numbers and coherence levels.

Figure 8 shows the differential interferograms of the selected patch for look numbers  $L=3, 12$  and  $24$ ,

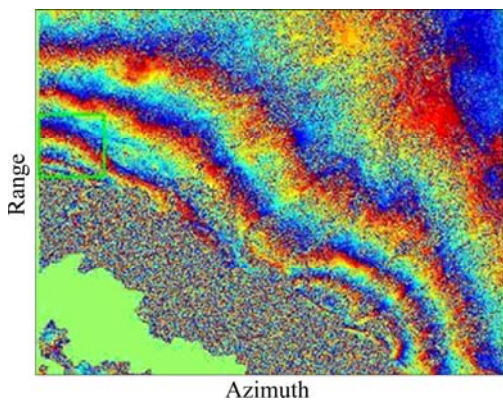


**Fig. 7** Geocoded differential interferogram of Wenchuan, China

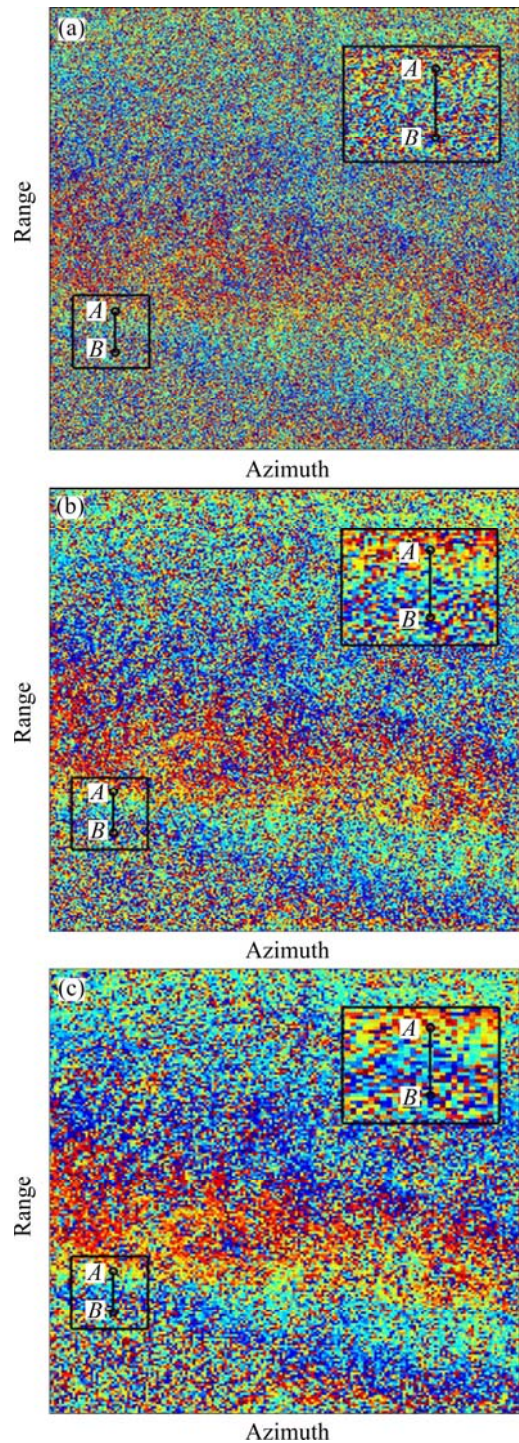


**Fig. 8** Selected interferogram patch for look numbers  $L=3$  (a),  $12$  (b) and  $24$  (c)

respectively. A profile named  $AB$  located in the southwest of the selected area is chosen, whose length is 452.8 m and deformation is 11.8 cm (one fringe). The deformation gradient along the profile is then  $0.26 \times 10^{-4}$  (i.e.,  $0.236/(2 \times 452.8)$ ). For look number  $L=3$ , the differential interferogram is seriously influenced by noise and the outlines of the deformation fringe are quite fuzzy. When look number  $L=12$ , the outlines of the fringe

become clear but the fringe is not continuous. The outlines are clearer and the fringe becomes continuous when look number  $L=24$ . The mean coherence and deformation gradient along this selected profile are  $\gamma=0.2535$  and  $D_{AB}=0.26\times 10^{-4}$ , respectively, as plotted in Fig. 9 with blue asterisk. The points locate within the green wedge while outside the red and blue wedge lines, which implies that the given deformation gradient can only be detected with look number  $L=24$ . The results demonstrate that the DDG model works in this case.

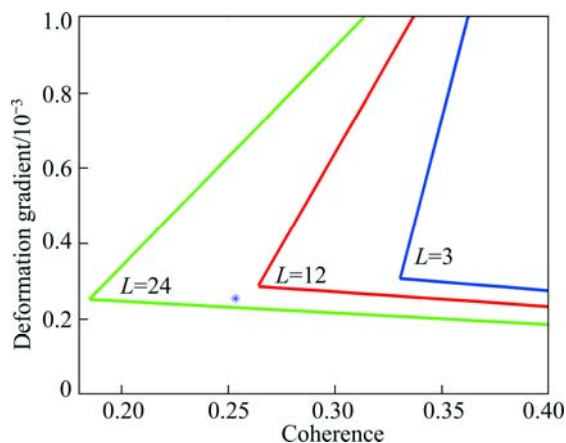


Fig. 9 Result of model validation

## 5 Conclusions

1) Generalized empirical functional models of the maximum and minimum DDG for PALSAR were established. In the generalization, the functional relationships among the slopes  $K_{\max}(L)$ ,  $K_{\min}(L)$  and the look number  $L$  were explored and modeled, and the final maximum and minimum DDG models therefore incorporated both the coherence and the look number.

2) The new model was validated with a PALSAR pair of Wenchun, China. The results showed that the new model works well in judging whether the deformation gradient can be detected by D-InSAR technology or not.

3) There are still some shortcomings. For example, the fringe detectability is decided based on visual analysis, and the relationship between pixel size and look number is based on experience, both being somewhat subjective. Nevertheless, we can still collect the deformation and coherence information in advance, and judge whether it can be monitored by D-InSAR. In a word, the results in this work can help researchers to choose PALSAR data and to configure processing parameters, and also benefit the interpretation of the surface deformation measured by PALSAR.

## References

- [1] HU J, LI Z W, ZHANG L, DING X L, ZHU J J, SUN Q, DING W. Correcting ionospheric effects and monitoring two-dimensional displacement fields with multiple-aperture InSAR technology with application to the Yushu earthquake [J]. *Science China: Earth Sciences*, 2012, 55(12): 1961–1971.
- [2] XING Xue-min, ZHU Jian-jun, WANG Yong-zhe, YANG Ya-fu. Time series ground subsidence inversion in mining area based on CRInSAR and PSInSAR integration [J]. *Journal of Central South University*, 2013, 20: 2498–2509.
- [3] LI Jia, LI Zhi-wei, ZHU Jian-jun, DING Xiao-li, WANG Chang-cheng. Deriving surface motion of mountain glaciers in the Tuomuer-Khan Tengri Mountain ranges from PLASAR images [J]. *Global and Planetary changes*, 2013, 101: 61–71.
- [4] GATELLI F. The wavenumber shift in SAR Interferometry [J]. *IEEE Transactions on Geoscience and Remote Sensing*, 1994, 32(4): 855–865.
- [5] SUN Qian, LI Zhi-wei, ZHU Jian-jun, DING Xiao-li, HU Jun, XU Bing. Improved Goldstein filter for InSAR noise reduction based on local SNR [J]. *Journal of Central South University*, 2013, 20(7): 1896–1903.
- [6] DING Xiao-li, LI Zhi-wei, ZHU Jian-jun, FENG Guang-cai, LONG Jiang-ping. Atmospheric effects on InSAR measurements and their mitigation [J]. *Sensors*, 2008, 8: 5426–5448.
- [7] MICHEL R, AVOUAC J P, TABOURY J. Measuring near field coseismic displacements from SAR images: Application to the Landers earthquake [J]. *Geophys Res Lett*, 1999, 26: 3017–3020.
- [8] MASSONNET D, FEIGL K. Radar interferometry and its application to changes in the earth's surface [J]. *Review of Geophysics*, 1998, 36(4): 441–500.
- [9] BARAN I S, STEWART M, CLAESSENS S. A new functional model for determining minimum and maximum detectable deformation gradient resolved by satellite radar interferometry [J]. *IEEE Transactions on Geoscience and Remote Sensing*, 2005, 43(4): 675–682.
- [10] LEE J S, HOPPEL K W, MANGO S A, MILLER A R. Intensity and phase statistics of multilook polarimetric and interferometric SAR imagery [J]. *IEEE Transactions on Geoscience and Remote Sensing*, 1994, 32(5): 1017–1028.
- [11] JIANG Mi, LI Zhi-wei. A study on the maximum and minimum detectable deformation gradients resolved by InSAR [J]. *Chinese Journal of Geophysics*, 2009, 52(7): 1715–1724. (in Chinese)
- [12] ROSENQVIST A, SHIMADA M, ITO N, WATANABE M. ALOS PALSAR: A pathfinder mission for global-scale monitoring of the environment [J]. *IEEE Transactions on Geoscience and Remote Sensing*, 2007, 45(11): 3307–3316.
- [13] LEE J S, PAPANASSIOU K P, AINSWORTH T L, GRUNES M R, REIGBER A. A new technique for noise filtering of SAR interferometric phase images [J]. *IEEE Transactions on Geoscience and Remote Sensing*, 1998, 36(5): 1456–1465.
- [14] BARAN I. Advanced satellite radar interferometry for small-scale surface deformation detection [D]. Australia: Curtin University of Technology, 2004.
- [15] TROUVE E, CARAMMA H, MAITRE H. Fringe detection in noisy complex interferograms [J]. *Applied Optics*, 1996, 35(20): 3799–3806.

# PALSAR 可检测的最大/最小地表形变梯度的 统一函数模型

王琪洁<sup>1</sup>, 李志伟<sup>1</sup>, 杜亚男<sup>1</sup>, 谢荣安<sup>2</sup>, 张杏清<sup>2</sup>, 蒋 弥<sup>1</sup>, 朱建军<sup>1</sup>

1. 中南大学 地球科学与信息物理学院, 长沙 410083;

2. 广东省地质测绘院, 广州 510800

**摘 要:** 基于相干性和离散视数, 建立 PALSAR 干涉可检测的最大和最小形变梯度的经验函数模型。在此基础上, 采用最小二乘回归的方法拟合模型系数, 建立关于相干性和视数两个参数的统一函数模型。利用汶川地区的 PALSAR 数据进行实验, 结果表明该模型能够准确判别地表变形能否被 D-InSAR 技术检测到。研究结果可以帮助研究人员准确选择 PALSAR 数据和合理配置其干涉处理参数, 对解释地表形变结果也具有重要的价值。

**关键词:** PALSAR; D-InSAR; 形变梯度; 相干性; 视数; 函数模型

(Edited by Sai-qian YUAN)